Stress-driven sliding of asymmetric grain boundaries

Kunqing Ding[1], Yin Zhang[2], Lihua Wang[3], Xiaodong Han[3], Ting Zhu[1,*]

[1]Woodruff School of Mechanical Engineering, Georgia Institute of Technology, Atlanta, Georgia 30332, USA

[2]School of Mechanics and Engineering Science, Peking University, 100871, Beijing, China

[3]Institute of Microstructure and Property of Advanced Materials, Beijing Key Lab of Microstructure and Property of Advanced Materials, Beijing University of Technology, Beijing, 100124, China

Abstract

Grain boundary (GB) deformation significantly influences the mechanical response of polycrystalline materials, yet most atomic-scale studies have focused on special coincidence site lattice (CSL) boundaries. In contrast, engineering polycrystals are typically dominated by asymmetric non-CSL GBs. In face-centered cubic (FCC) metals, these boundaries often undergo sliding with minimal migration, a process primarily mediated by step-free GB dislocations. Motivated by recent in situ atomic-resolution experiments, we use atomistic modeling to investigate stress-driven sliding in asymmetric, non-CSL tilt GBs. Our results reveal that sliding is governed by the glide of extrinsic GB dislocations and their interactions with intrinsic ones. Despite the structural complexity of non-CSL boundaries, we identify the operative slip geometries of these extrinsic dislocations. Furthermore, we uncover a kink-pair mechanism of GB dislocation glide that acts as the primary rate-controlling step for sliding kinetics. These findings provide critical atomic-scale insights into asymmetric tilt GB deformation and establish a mechanistic foundation for understanding GB-mediated plasticity in engineering polycrystals.

*Corresponding author: ting.zhu@me.gatech.edu

1. Introduction

Grain boundaries (GBs) serve as critical interfaces between adjacent grains in polycrystalline materials, profoundly influencing their mechanical properties such as yield strength, ductility, creep resistance, and fracture toughness [1]. In fine-grained and nanocrystalline metals, where the GB volume fraction is substantial, GB-mediated plasticity can become the dominant deformation mode [2]. While atomic-scale microscopy and modeling have significantly advanced our understanding of these interfaces [3-10], most investigations have historically targeted special coincidence site lattice (CSL) GBs [11], particularly symmetric tilt GBs, due to their crystallographic simplicity and computational tractability [12].

In contrast, engineering polycrystals are predominantly composed of asymmetric non-CSL GBs [13]. In face-centered cubic (FCC) materials, asymmetric tilt GBs featuring at least one low-index plane (e.g., {111} or {100}) are frequently observed [14-16]. Under applied stress, these boundaries often exhibit sliding with minimal migration, a process governed by step-free GB dislocations rather than the commonly studied step-bearing GB disconnections [8]. This distinction prompts several fundamental questions: What determines the translation periodicity of these complex interfaces? What is the minimum relative displacement between adjoining grains (i.e., a displacement-shift complete [1]) that preserves the GB structure? How do interactions between intrinsic and extrinsic GB dislocations [3] dictate stress-driven sliding?

To address these questions, we employ atomistic modeling to characterize stress-driven sliding in asymmetric tilt GBs in FCC bicrystals, motivated by recent in situ atomic-resolution experiments [8]. Our results demonstrate that: (1) The GB translation periodicity $\boldsymbol{\lambda}$ is governed by the spacing of intrinsic GB misfit dislocations. (2) The slip vector $\mathbf{b}$ corresponding to a displacement-shift complete is dictated by the lattice periodicity of the grain's low-index surface. (3) Extrinsic GB dislocations carrying $\mathbf{b}$ glide in discrete, structure-preserving increments of $\boldsymbol{\lambda}$ and dissociate into partial dislocations. It should be emphasized that $\mathbf{b}$ and $\boldsymbol{\lambda}$ usually differ for complex GB structures [3]. Furthermore, we show that the glide of these extrinsic GB dislocations occurs through a highly localized kink-pair mechanism. This mechanism serves as the primary rate-limiting step for GB sliding kinetics. These findings provide a mechanistic understanding of plasticity in structurally complex GBs in engineering polycrystals.

2. Model and results

2.1 Structure of asymmetric tilt GBs

We investigated an asymmetric tilt GB in an FCC Ni bicrystal. Its GB structure closely resembles that in FCC Pt observed by Wang et al. [8] through in situ nanomechanical testing with high-resolution transmission electron microscopy (HRTEM). Interatomic interactions were modeled using the angular-dependent potential (ADP) for Ni [17], which stabilizes GB structures consistent with experimental observations. The system was relaxed using conjugate gradient energy minimization in LAMMPS [18], and atomic configurations were visualized with OVITO [19]. Fig. 1a-1c show the atomic structure of this asymmetric $\langle 110 \rangle$ tilt GB (21.8° misorientation) following conjugate gradient relaxation. Specifically, Fig. 1a presents the atomic structure of the bicrystal, which measures 13 × 18 × 1 nm^3 and contains 21,821 atoms. Grains G1 and G2 are aligned along the $[\bar{1}10]$ zone axis. The G2 surface is composed of a flat, close-packed (111) plane, whereas the G1 surface consists of high-index (331) planes. Periodic boundary conditions are applied along the out-of-plane $[\bar{1}10]$ direction, while the lateral, top and bottom surfaces are traction-free. For comparison, Fig. 1d-1f present HRTEM images of the analogous experimental GB [8], where grains G1 and G2 are aligned along the $[\bar{1}10]$ zone axis. In these micrographs, each white spot represents a $[\bar{1}10]$ atomic column. The G2 grain surface exposes a flat, close-packed (111) plane, whereas the G1 side comprises a high-index (331) plane characterized by single-atomic-height steps separated by short (111) and $(1\bar{1}1)$ facets (marked in Fig. 1d). This configuration constitutes an asymmetric, non-CSL tilt GB, distinct from the idealized CSL boundaries in typical atomistic simulations.

To determine the GB translation periodicity, we analyzed the structural units within the boxed region of Fig. 1a (detailed in Fig. 1b). While the boundary appears to repeat as a sequence of regular (blue) and distorted (red) pentagon units in Fig. 1b, these 2D profiles are insufficient to define the true periodicity due to the 3D registry of the interface. Fig. 1c provides a top-down view of the G1 (black) and G2 (white) surface atoms, clarifying their relative positions along the $[\bar{1}10]$ zone axis. The G1 atoms occupy three-fold sites above the close-packed (111) surface of G2. As shown in the out-of-plane registry along $[\bar{1}10]$ (Fig. 1c), atoms A and C share identical out-of-plane positions, while atom B is offset to occupy a favorable hollow site on the (111) surface of G2. As a result, the blue pentagon units associated with atoms A and B possess distinct 3D

configurations. The in-plane translation complete condition is therefore satisfied only over a sequence of four distinct pentagon units (distinguished by color and line style in Fig. 1b). This dictates an in-plane translation period $\boldsymbol{\lambda}$ corresponding to $5/2[\bar{1}\bar{1}2](111)$ relative to the G2 lattice.

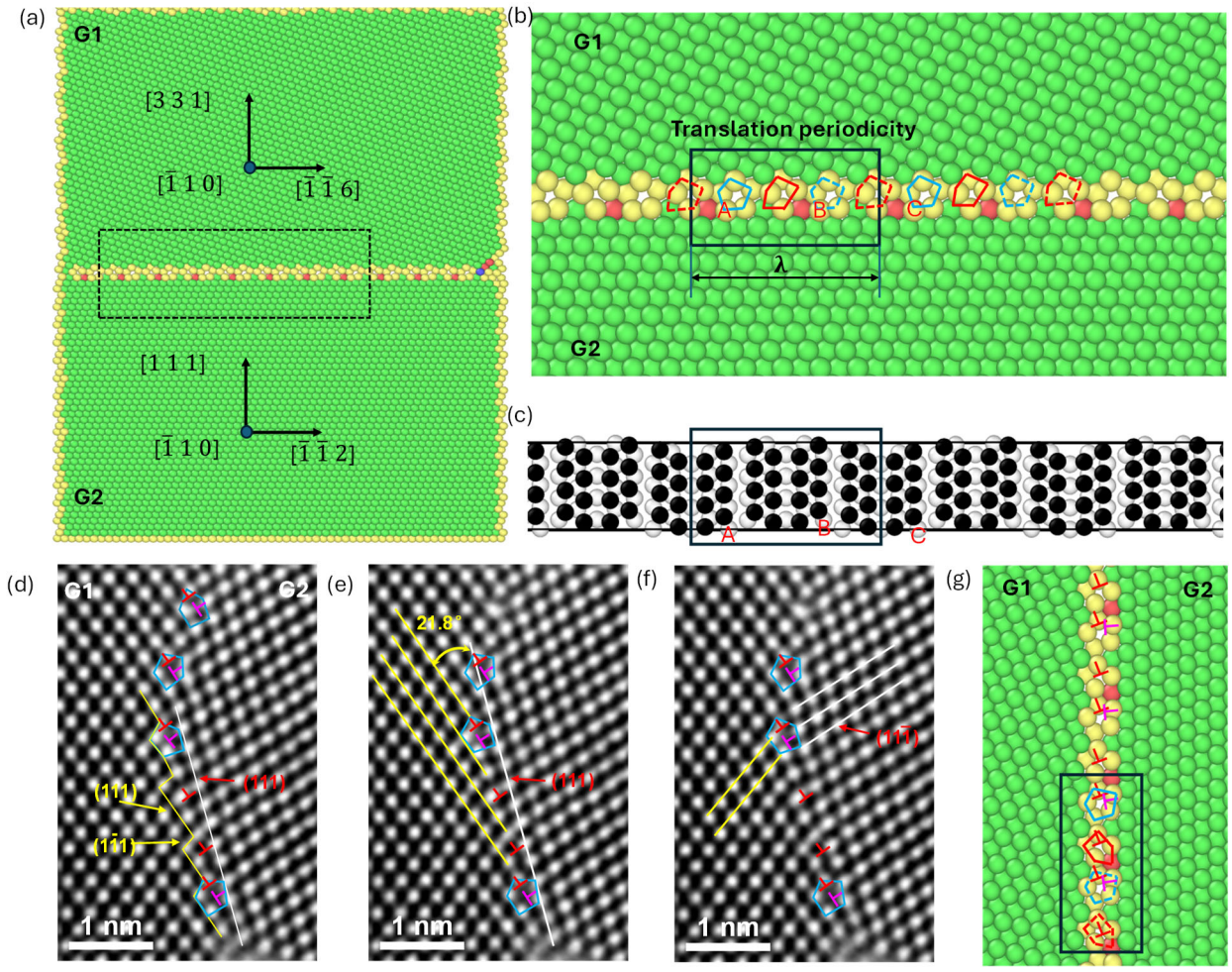

Fig. 1. Structure of an asymmetric ⟨110⟩ tilt GB with a misorientation of 21.8°. (a) Atomic model of the Ni bicrystal, where the upper grain G1 exposes a (331) surface and the lower grain G2 exposes a flat, close-packed (111) surface. Atoms are colored by common neighbor analysis: FCC (green), hexagonal close-packed (HCP, red), and others (yellow). (b) Enlarged view of the boxed region in (a). The translation period $\boldsymbol{\lambda}$ (solid box) spans four distinct pentagon-shaped structural units (outlined with different line colors and types). (c) Top-down view showing only grain surface atoms: G1 (black) and G2 (white). The out-of-plane registry for atoms A, B, and C (labeled in (a)) is shown along the $[\bar{1}10]$ direction. (d) HRTEM image of an analogous GB in a Pt bicrystal, adapted from Wang et al. [8]. G1 shows a high-index (331) surface with single-atomic-height steps separated by short (111) and $(1\bar{1}1)$ facets (yellow lines), while G2 presents a flat (111) grain surface (white line). (e, f) Identification of intrinsic GB dislocations in the experimental GB: red symbols ⊥ mark terminations of extra half-planes of misorientation dislocations, while pink

symbols ⊥ mark misfit dislocations. (g) Atomic GB model annotated over one translation period (solid box), showing both pentagon units and the corresponding intrinsic GB dislocations.

What structural factors govern the translation periodicity along an asymmetric tilt GB? This periodicity is mainly controlled by the spacing of intrinsic misfit dislocations, which form to accommodate atomic misalignment across the asymmetric boundary. In the experimental GB shown in Fig. 1d-1f, two distinct types of intrinsic GB dislocations are identified: one (red "⊥" symbols) accommodates the lattice misorientation with a Burgers vector of $1/2[110]$, while the other (pink "⊥" symbols) accommodates the lattice misfit across the boundary with a Burgers vector of $1/2[0\bar{1}1]$. These dislocations frequently pair to form a GB Lomer lock with a combined Burgers vector of $1/2[101]$. The core of a GB Lomer lock appears as a regular pentagon, whereas that of an isolated misfit dislocation appears as a distorted pentagon. Although the experimental GB in Fig. 1d-1f is not perfectly periodic due to the presence of a (331) surface step [8], the model in Fig. 1g reveals a repeating sequence of alternating GB Lomer locks and misfit dislocations. By doubling the repeat spacing of these misfit dislocations, a full translation periodicity is established, consistent with the out-of-plane atomic registry discussed earlier.

2.2 Uniform GB sliding

Using the bicrystal model in Fig. 1a, we studied uniform GB sliding by applying incremental in-plane shear displacements to the upper surface relative to the lower surface, followed by relaxation via conjugate gradient energy minimization after each increment. This study allows us to determine the slip vector **b** of the GB structure. Fig. 2a provides a magnified view of the GB region during uniform sliding, illustrating the leftward translation of grain G1 relative to G2. Our analysis reveals that a full displacement-shift complete is achieved through a sequence of four discrete sliding steps. Fig. 2b1-2b5 present the top-down relative displacement maps for nearest-neighbor atom pairs across the GB at each step. Fig. 2b5 repeats Fig. 2b1, confirming that a complete structural shift is reached after the four-step sequence shown in Fig. 2b1-2b4. Within each map, the relative displacements for two neighboring atomic columns (brown box) are identical; four such column pairs constitute a single periodic unit (black box), consistent with the translation periodicity identified in Fig. 1b. In Fig. 2b1-2b4, the average relative displacement within each periodic unit is approximately $1/8[\bar{1}\bar{1}2](111)$. Fig. 2b6 displays the cumulative relative displacement map for all nearest-neighbor atom pairs across the GB; minor deviations

from the exact lattice period $1/2[\bar{1}\bar{1}2](111)$ arise due to additional elastic deformation caused by applied shear loading. Therefore, the slip vector **b** for this asymmetric GB is determined to be $1/2[\bar{1}\bar{1}2](111)$, which is realized via four sequential increments (Fig. 2b1-2b4), each involving a partial slip vector of $1/8[\bar{1}\bar{1}2](111)$.

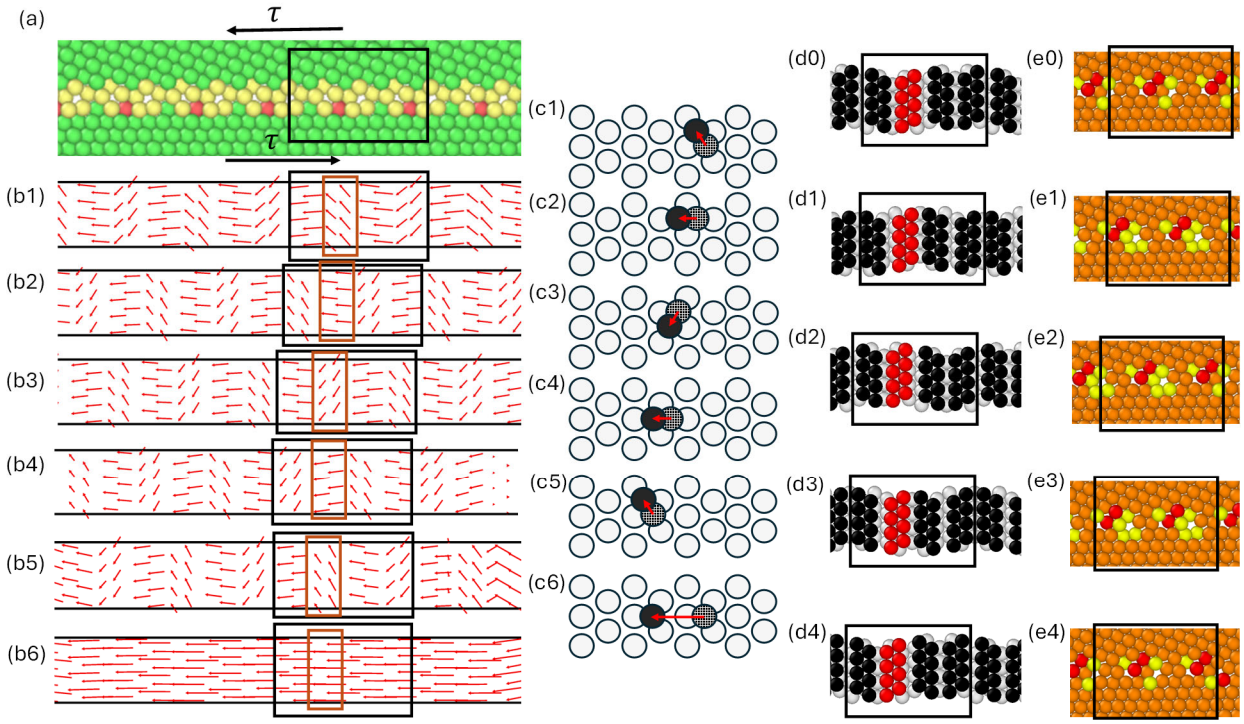

Fig. 2. Uniform GB sliding under applied shear stress τ. (a) Magnified view of the GB region, with one translation period indicated by a solid box. (b) Top-down relative displacement maps for nearest-neighbor atom pairs across the GB during four sequential sliding steps (b1-b4). The map in (b5) repeats (b1), confirming that a displacement-shift complete is achieved after the four steps. (b6) shows the cumulative relative displacement map obtained by summing (b1-b4). (c) Schematics of a representative G1 surface atom progressing through four sequential sliding steps (c1-c4) to reach the displacement-shift complete state (c5). The cumulative relative displacement of this atom is illustrated in (c6). (d) Top-down positions of G1 and G2 surface atoms before and after each sliding step (d0-d4). (e) $[\bar{1}10]$ views of the corresponding GB structures in (d). Atoms are colored by coordination number N: 12 (orange, perfect FCC structure), 13 (red), and 11 (yellow).

What determines the slip vector of an asymmetric tilt GB during sliding without migration? In asymmetric tilt GBs featuring a flat, close-packed (111) grain surface, the slip vector is fundamentally governed by the lattice periodicity of the (111) surface, which possesses a two-fold rotational symmetry axis normal to the surface plane [3]. Each surface atom of grain G1 traverses

four sequential steps to achieve a displacement-shift complete of $1/2[\bar{1}\bar{1}2](111)$, a vector consistent with the in-plane lattice periodicity of the G2 (111) surface. Fig. 2c1-2c4 illustrate a G1 surface atom moving in $1/6\langle 112\rangle$ increments between three-fold sites (indicated by gridded to solid circles) atop the G2 (111) plane. After four steps, the atom returns to an equivalent site (Fig. 2c5). The total relative displacement (Fig. 2c6) confirms a cumulative slip vector **b** of $1/2[\bar{1}\bar{1}2](111)$. While each incremental step corresponds to a specific variant of the $1/6\langle 112\rangle$ family, neighboring atomic columns within a single GB periodic unit follow different $1/6\langle 112\rangle$ variants. Nonetheless, the cumulative slip vector of $1/2[\bar{1}\bar{1}2](111)$ remains dictated by the G2 (111) lattice periodicity.

Top-down views of the G1 and G2 surface atoms during these four sliding steps are shown in Fig. 2d0-2d4. By Fig. 2d4, the atomic pattern within the GB periodic unit (black box) repeats that in Fig. 2d0 but is translated leftward by $1/2[\bar{1}\bar{1}2](111)$, confirming the displacement-shift complete. Fig. 2e0-2e4 present $[\bar{1}10]$ views of the same steps shown in Fig. 2d0-2d4, with atoms colored by coordination number. In Fig. 2e4, the periodic unit (black box) likewise repeats that in Fig. 2e0 with a $1/2[\bar{1}\bar{1}2](111)$ shift. Intermediate states (Fig. 2e1-2e3) exhibit an increase in miscoordinated atoms resulting from partial slips of $1/8[\bar{1}\bar{1}2](111)$. After the fourth step, the total sliding displacement of $1/2[\bar{1}\bar{1}2](111)$ restores the initial structure (Fig. 2e4). These miscoordinated atoms are primarily localized to the G1 and G2 surface layers (Fig. 2e1-2e3), where atoms undergo significant relative displacements; conversely, atoms within the grain interiors experience minimal rigid-body shifts of $1/8[\bar{1}\bar{1}2](111)$ per step.

2.3 Motion of extrinsic GB dislocations

We also investigated non-uniform sliding in the asymmetric tilt GB model shown in Fig. 1a. This process, mediated by the glide of extrinsic GB dislocations, is generally more favorable than uniform sliding [3]. Consistent with the slip geometry established during uniform sliding, an extrinsic GB dislocation with a full Burgers vector **b** $=1/2[\bar{1}\bar{1}2](111)$ advances by a GB structural period $\boldsymbol{\lambda} = 5/2[\bar{1}\bar{1}2](111)$ to preserve the boundary structure. This extrinsic dislocation dissociates into four partials, each carrying a partial Burgers vector of **b**/4 = $1/8[\bar{1}\bar{1}2](111)$. The preexisting intrinsic GB dislocations (Fig. 1g) hinder the motion of these extrinsic partial dislocations, thereby imposing energy barriers that control the kinetics of non-uniform GB sliding.

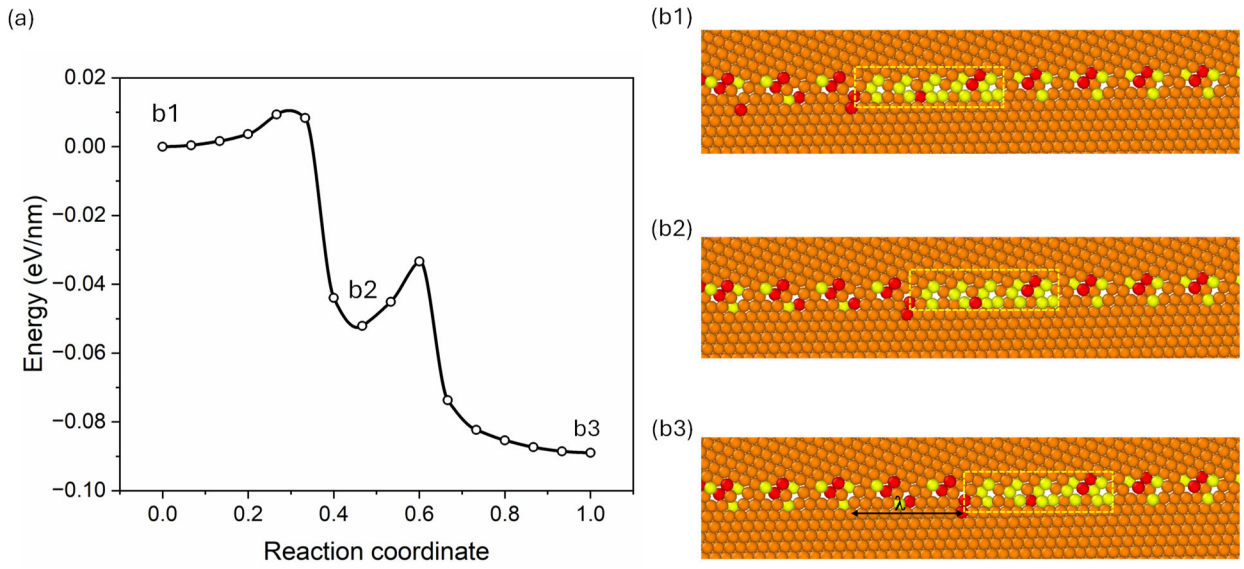

Fig. 3. 2D NEB results for a unit step of thermally activated glide of the leading partial of an extrinsic GB dislocation. (a) MEP under an applied shear stress τ of 59.7 MPa. Three local energy minima are labeled b1-b3, indicating that one unit glide step proceeds through two sequential sub-steps (b1→b2 and b2→b3). (b) Atomic configurations (b1-b3) correspond to these minima in (a). Atoms are colored by coordination number, as in Fig. 2e. The core of the leading partial, highlighted by a yellow dashed box, is composed primarily of miscoordinated (yellow) atoms and moves by a GB structural period $\boldsymbol{\lambda}$ from (b1) to (b3).

At finite temperatures, dislocation glide occurs via thermally activated steps when the applied shear stress is below the athermal stress, at which the energy barrier vanishes and motion becomes instantaneous. To characterize this thermally activated process, we employed the stress-controlled nudged elastic band (σ-NEB) method [20] and first modeled a GB dislocation within a thin bicrystal (~1 nm thick). This setup constrains the dislocation to 2D motion, yielding identical atomic displacements along each $[\bar{1}10]$ column (Fig. 3a-3b). To prepare for the σ-NEB calculation, the leading partial of an extrinsic dislocation was introduced by imposing a relative displacement [21] of $1/8[\bar{1}\bar{1}2](111)$ between atom pairs across the GB in Fig. 1a, on the left side of the intended dislocation core, followed by structural relaxation. The resulting core (yellow box in Fig. 3b1) spans about five pentagon units and consists primarily of miscoordinated atoms. The GB structure trailing the partial dislocation core differs from that ahead of the core, exhibiting variations in atomic coordination and out-of-plane registry; the atomic configurations of single

and double GB partial dislocations will be compared in the Discussion section. During each σ-NEB calculation, a constant leftward force was applied to atoms in the top five layers, while the bottom five layers were fixed, thereby maintaining a constant shear stress during relaxation.

For example, under an applied shear stress τ of 59.7 MPa (below the athermal stress of 165 MPa), the σ-NEB calculation converges to a minimum energy path (MEP) for a single rightward glide step of the extrinsic GB partial dislocation. As shown in Fig. 3a, the MEP reveals that this glide proceeds via two sequential sub-steps, evidenced by two successive energy barriers and three local minima. The atomic configurations corresponding to these minima are shown in Fig. 3b1-b3. From the initial to the final state, atom pairs within the partial dislocation core undergo a relative shift equal to the partial Burgers vector $1/8[\bar{1}\bar{1}2](111)$. This results in a rightward core translation by one GB structural period $\boldsymbol{\lambda} = 5/2[\bar{1}\bar{1}2](111)$ (Fig. 3b3). This unit glide step proceeds via two sequential sub-steps, as evidenced by the intermediate local minimum (b2 in Fig. 3a) and the corresponding core configuration in Fig. 3b2. The first sub-step displaces the core by $\boldsymbol{\lambda}/2$, while the second completes the motion with the remaining $\boldsymbol{\lambda}/2$. This stepwise glide mechanism drives non-uniform GB sliding through repeated glide steps of these extrinsic GB partial dislocations.

The 2D σ-NEB calculation in Fig. 3a reveals two energy barriers, each scaling linearly with crystal thickness. Since such barriers cannot increase indefinitely with thickness, a localized 3D mechanism reduces them. Our 3D σ-NEB calculation identifies a kink-pair mechanism, uncommon in FCC metals [20], that enables the glide of an extrinsic GB partial dislocation in the bicrystal shown in Fig. 1a. The bicrystal was extended along the out-of-plane $[\bar{1}10]$ direction to 17.9 nm, yielding a thicker GB structure with 392,778 atoms. Fig. 4a presents the corresponding MEP under a shear stress of 23.9 MPa. The associated displacements of G1 surface atoms, reflecting the relative displacements across the boundary, are displayed in Fig. 4b1-b4. As in the 2D σ-NEB case (Fig. 3), the 3D unit glide step involves two sequential sub-steps, each mediated by a kink pair. In the first sub-step, a kink pair (Fig. 4b1) forms in the dislocation core near the first saddle point (b1 in Fig. 4a). The two kinks migrate in opposite directions until the dislocation restores a straight configuration at an intermediate minimum (Fig. 4b2; b2 in Fig. 4a). The second sub-step follows, with a second kink pair (Fig. 4b3) forming near the second saddle point (b3 in Fig. 4a). This process progresses to the final minimum (b4 in Fig. 4a), again resulting in a straight dislocation core (Fig. 4b4). The saddle points b1 and b3 in Fig. 4a correspond to energy barriers

of 0.37 eV and 0.49 eV, respectively. The latter represents the rate-limiting step, defining the activation energy E_a for the glide process and, consequently, the kinetics of GB sliding.

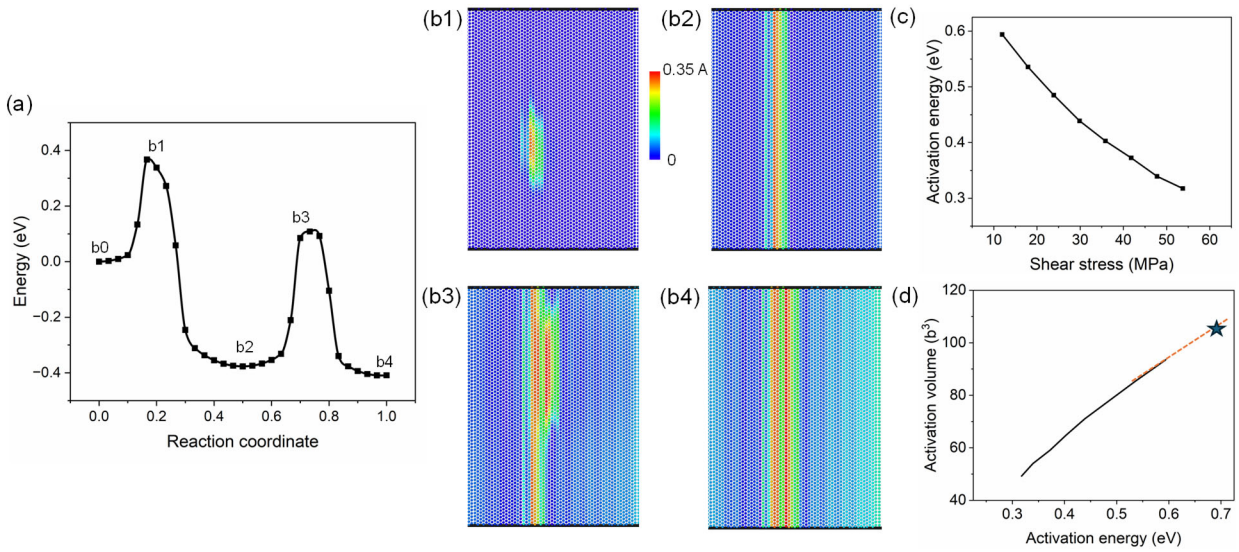

Fig. 4. 3D NEB results for a unit step of thermally activated glide of the leading partial of an extrinsic GB dislocation. (a) MEP under an applied shear stress of $\tau = 23.9$ MPa. (b) Contour map of sliding displacement Δd of G1 surface atoms, referenced to the configuration (not shown) at the initial local energy minimum (denoted as b0). The corresponding energies of states b0-b4 are indicated in (a). (c) Activation energy E_a as a function of applied shear stress τ. (d) Activation volume V_a as a function of activation energy E_a. The data are extrapolated to higher E_a values (red dashed line) to obtain the characteristic V_a value (marked by a star) at $E_a = 0.7$ eV.

We further calculated the activation energy E_a for the kink-pair mechanism across a range of shear stresses τ (Fig. 4c). A characteristic E_a value of 0.7 eV corresponds to a typical laboratory strain rate of 10^{-3} s^{-1} at room temperature [20]. From Fig. 4c, the required τ is less than 10 MPa when $E_a = 0.7$ eV, indicating that the glide of this extrinsic GB partial dislocation can be activated under relatively low driving stresses. Due to stability limits, 3D σ-NEB calculations did not converge for higher E_a values. In addition to the activation energy, we determined the activation volume, defined as $V_a = -\partial E_a/\partial \tau$ [22]. Fig. 4d shows the V_a versus E_a curve (black solid line) derived from the E_a versus τ plot in Fig. 4c, with extrapolation to higher activation energies (indicated by the red dashed line). For $E_a = 0.7$ eV, V_a is approximately $110b_L^3$ (star in Fig. 4d), where b_L is the Burgers vector length of a lattice dislocation in FCC Ni. These atomistically

determined activation volumes can be compared with experimental measurements [23] to assess strain rate sensitivity and identify the rate-limiting process in polycrystals under typical laboratory strain rate conditions (~10^{-3} s^{-1}) . To achieve this, further model development is required to account for intragranular deformation processes, thereby bridging the gap between activation volumes derived from bulk polycrystal experiments and those associated with local GB-mediated events [24].

3. Discussion

3.1 GB partial dislocations

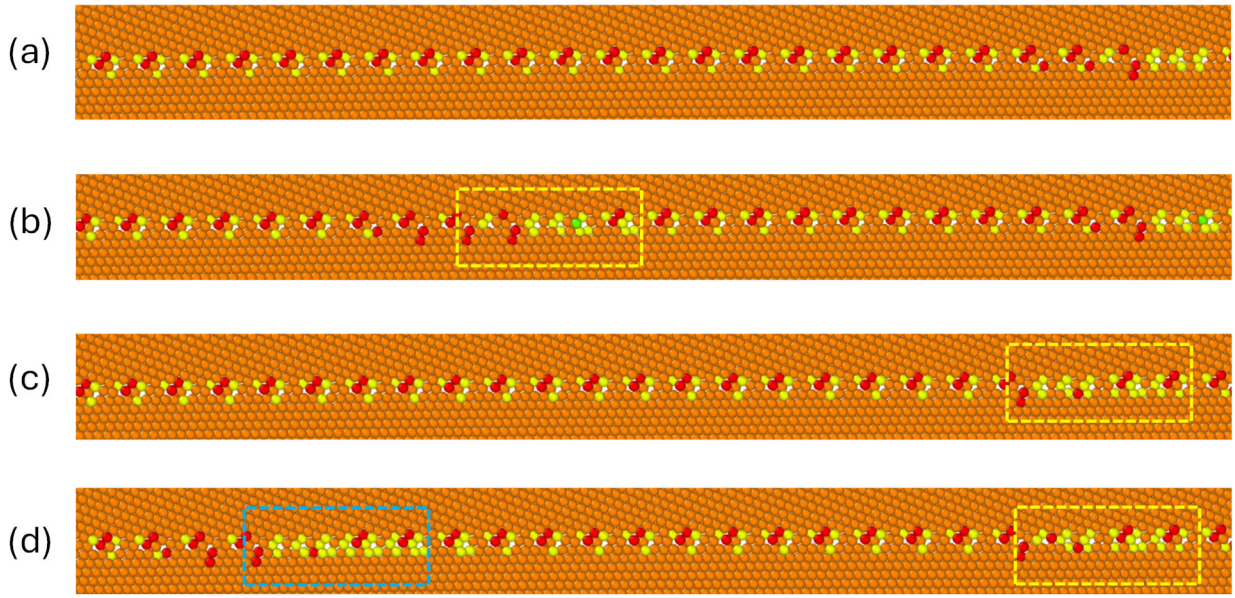

Fig. 5. Non-uniform sliding of an asymmetric ⟨110⟩ tilt GB with a 21.8° misorientation (same structure as Fig. 1a) via the sequential glide of two partials of an extrinsic GB dislocation. Atoms are colored by coordination number, as in Fig. 2e. (a) Initial GB structure prior to sliding, with no extrinsic GB dislocations present. (b) The first partial of an extrinsic GB dislocation, with a partial Burgers vector of $1/8[\bar{1}\bar{1}2](111)$, is introduced as the bicrystal is subjected to applied shear stress; the core of this partial is highlighted with a yellow box. (c) The first partial glides rightward under increasing shear stress. (d) The second partial, with a partial Burgers vector of $1/8[\bar{1}\bar{1}2](111)$, is introduced under a further increase in shear stress; its core is marked with a blue box.

To investigate the structure of coexisting partials of an extrinsic GB dislocation, we sequentially introduced two such partials into the GB shown in Fig. 5a. First, we imposed a locally controlled shift [21] of $1/8[\bar{1}\bar{1}2](111)$ across the boundary on the left side of the core of the first intended partial dislocation, followed by structural relaxation (Fig. 5b). Subsequently, we increased the applied shear stress to displace this partial to the right end of the bicrystal (Fig. 5c). Next, we imposed a locally controlled shift of $1/8[\bar{1}\bar{1}2](111)$ across the boundary at the left side of the second intended partial core, followed by structural relaxation (Fig. 5d). Due to the repulsive interaction between the two partials, arising from their identical partial Burgers vectors, a longer GB is required. The corresponding bicrystal measures 33 × 18 × 1 nm^3 and contains 55,252 atoms, with the same crystal orientation as in Fig. 1a. This procedure can be extended to introduce four partials along a longer boundary, thereby forming a complete extrinsic GB dislocation.

3.2 Near-CSL

The translation periodicity **λ** of the general non-CSL tilt GB in Fig. 1b suggests the existence of a near-CSL structure. Conventional CSL GBs are strictly defined by a dichromatic map of two rigid, misoriented grains [6]. To account for more complex GBs, we extend this framework to general asymmetric tilt GBs using the near-CSL scheme [25]. This near-CSL is identified by allowing a small positional tolerance ($\sim 5\% b_{\mathrm{L}}$), which accounts for local atomic relaxations required during GB formation. As illustrated in Fig. 6, the dichromatic map for the bicrystal in Fig. 1a reveals a near-CSL motif with a diamond-shaped pattern (outlined in pink). Any GB plane aligned with a diagonal or an edge of this diamond pattern maintains structural periodicity. Specifically, the vertical and horizontal diagonals correspond to mirror planes for symmetric GBs of the same misorientation, while the yellow edge defines the asymmetric GB plane analyzed in Fig. 1a. Along this edge, the {331} surface of grain G1, characterized by four single-atomic-height steps separated by short {111} facets, interfaces with the close-packed {111} surface of grain G2. This configuration forms a repeating structural motif of four pentagon units at this asymmetric tilt GB, consistent with the analysis in Fig. 1g. This near-CSL scheme enables the construction of periodic structural units in complex non-CSL tilt GBs.

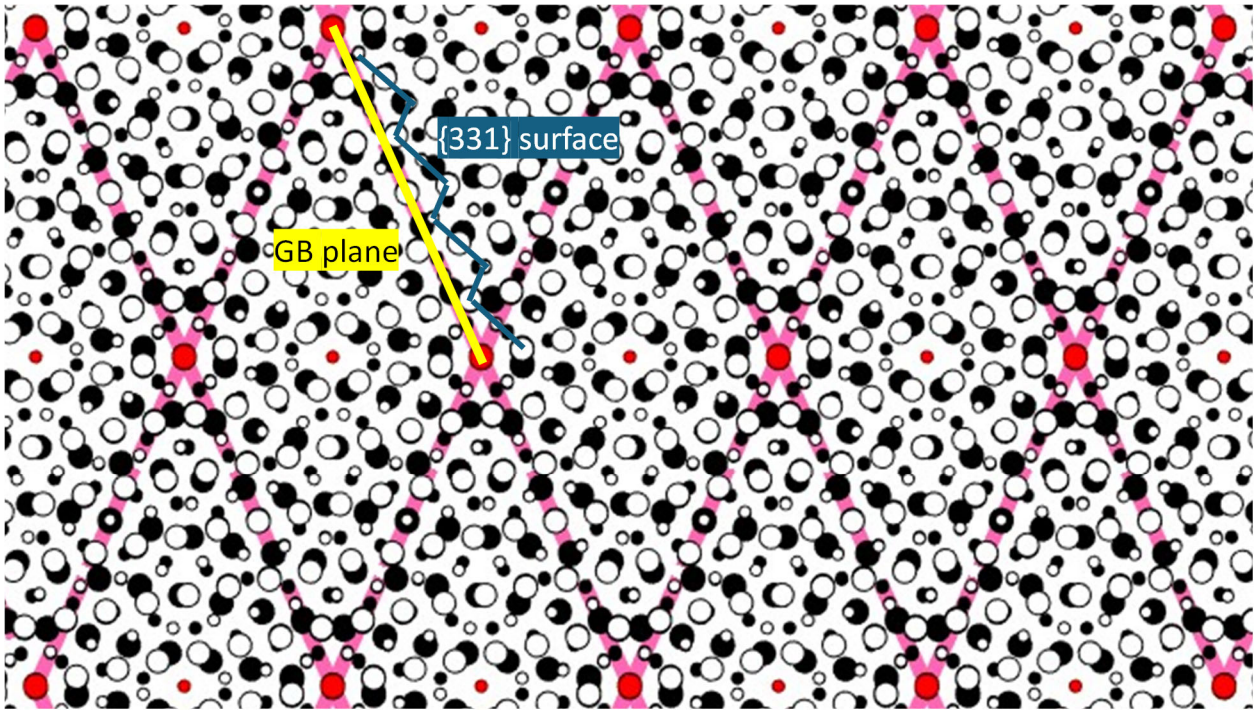

Fig. 6. Dichromatic map of the bicrystal in Fig. 1a, revealing a near-CSL ($\sum 40$) motif characterized by a diamond-shaped pattern outlined in pink. GB planes aligned with the edges (thick red lines) of the diamond pattern preserve the periodic structure. The yellow edge defines the GB plane in Fig. 1a, where the {331} grain surface interfaces with the close-packed {111} grain surface. The {331} surface consists of four single-atomic-height steps separated by narrow {111} facets (marked in blue).

3.3 An additional GB model

For asymmetric tilt GBs with larger misorientations, analysis based on discrete intrinsic GB dislocations is less directly applicable. However, identifiable misfit dislocations still emerge from the atomic disregistry across the boundary. For example, we examined a high-angle asymmetric $\langle 110 \rangle$ tilt GB previously characterized by Tian et al. [9]. This experimental GB exhibits a structure similar to that in Fig. 1d-f but with a larger misorientation of 54.7°. Based on this experimental structure, we developed a corresponding atomic model (Fig. 7a). In this Ni bicrystal model, both grains are aligned along the $[\bar{1}10]$ zone axis. The G2 surface is composed of a flat, close-packed (111) plane, while the G1 surface consists of a low-index (001) plane. The bicrystal measures 13 × 18 × 1 nm^3 and contains 22,079 atoms. In this case, the spacing of misfit dislocations defines a translation periodicity $\boldsymbol{\lambda}$ of $2[\bar{1}\bar{1}2](111)$ (Fig. 7b-7d), which differs from that in Fig. 1b.

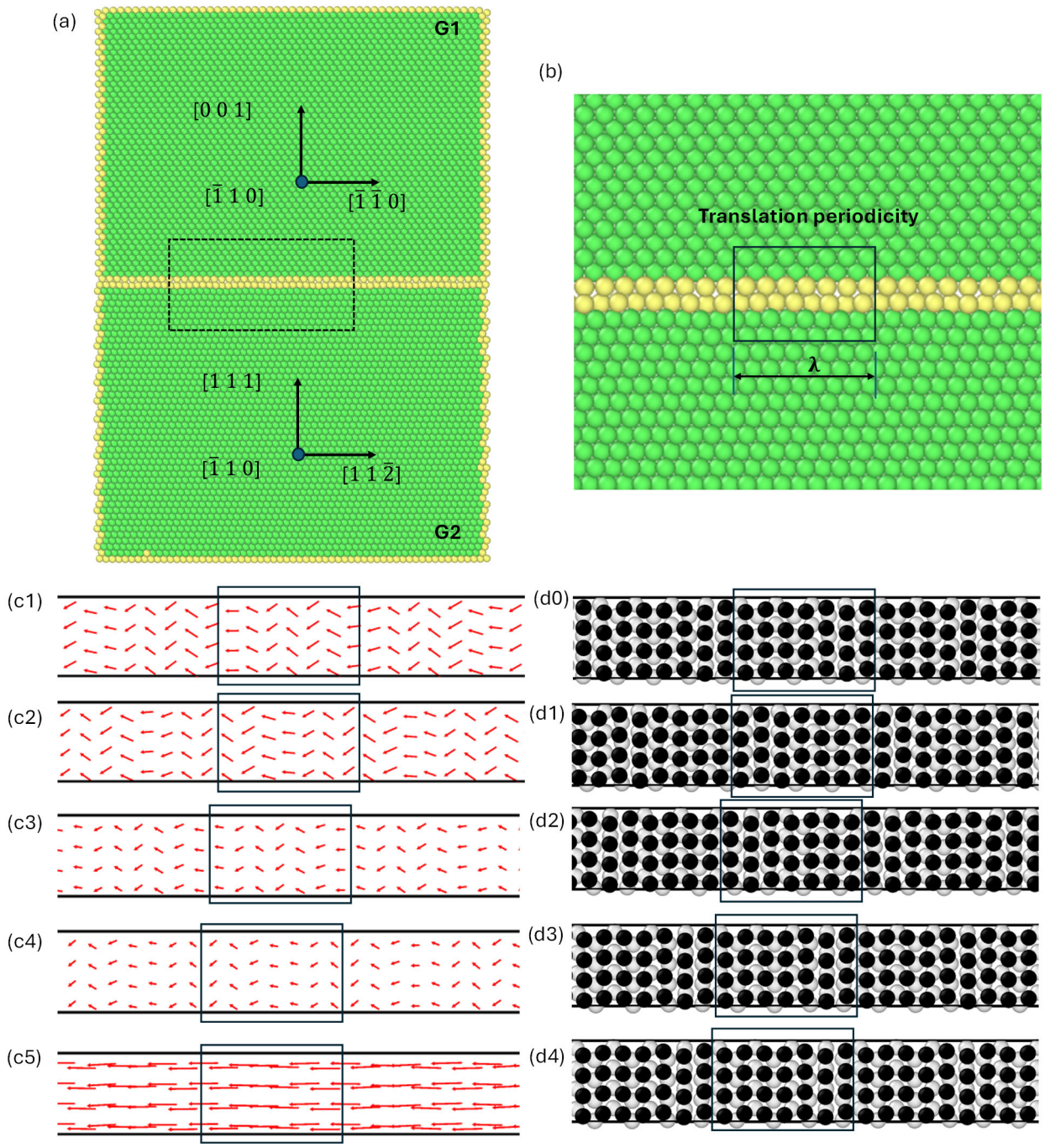

Fig. 7. An additional GB model: an asymmetric ⟨110⟩ tilt GB with a 54.7° misorientation. (a) Atomic GB model in a Ni bicrystal: upper grain G1 exposes a (001) surface, while lower grain G2 exposes a flat, close-packed (111) surface. (b) Enlarged view of the boxed region in (a). The translation periodicity λ is marked by the solid box. (c) Top-down relative displacement maps for nearest-neighbor atom pairs across the GB during four sequential sliding steps (c1-c4). (c5) shows the cumulative relative displacement map (sum of c1-c4). (e) Top-down positions of G1 and G2 surface atoms before and after each of the four sequential sliding steps.

GB sliding with a displacement-shift complete represents the minimum relative displacement required to preserve the GB structure. Does this slip vector remain the same if grain G1 has a different misorientation relative to G2 compared to the GB in Fig. 1a? To answer this question, we simulated uniform sliding using the Ni bicrystal model in Fig. 7. The slip vector was determined to be $1/2\langle 112\rangle\{111\}$ by evaluating the displacement-shift complete condition, which is also satisfied through four sequential sliding steps (Fig. 7c1-7c5). Although Fig. 7d1-7d5 reveal that not all surface atoms of grain G1 occupy ideal three-fold sites above the close-packed plane of grain G2, these structural deviations do not alter the slip vector. As long as the G2 surface remains a flat, close-packed {111} plane, it continues to dictate the sliding kinematics.

4. Conclusion

We have investigated stress-driven sliding in asymmetric tilt GBs in FCC crystals. Our results demonstrate that this process is mediated by the glide of extrinsic GB dislocations and their interactions with intrinsic ones. Despite the inherent structural complexity of these asymmetric interfaces, we identify the precise slip geometries of the participating dislocations. Furthermore, we uncover a kink-pair mechanism governing GB dislocation glide, which serves as the rate-limiting step for sliding kinetics. By advancing the atomistic understanding of structurally complex interfaces, this work establishes a mechanistic foundation for understanding GB-mediated plasticity in engineering polycrystals.

References

[1] A.P. Sutton, R.W. Balluffi, Interfaces in Crystalline Materials Oxford University Press, Oxford, UK, 1995.
[2] T. Zhu, J. Li, Ultra-strength Materials, Progress in Materials Science 55 (2010) 710-757.
[3] M.F. Ashby, Boundary defects, and atomistic aspects of boundary sliding and diffusional creep, Surface Science 31 (1972) 498-542.
[4] J.W. Cahn, Y. Mishin, A. Suzuki, Coupling grain boundary motion to shear deformation, Acta Materialia 54 (2006) 4953-4975.
[5] D.L. Medlin, K. Hattar, J.A. Zimmerman, F. Abdeljawad, S.M. Foiles, Defect character at grain boundary facet junctions: Analysis of an asymmetric $\Sigma = 5$ grain boundary in Fe, Acta Materialia 124 (2017) 383-396.
[6] J. Han, S.L. Thomas, D.J. Srolovitz, Grain-boundary kinetics: A unified approach, Progress in Materials Science 98 (2018) 386-476.
[7] T. Meiners, T. Frolov, R.E. Rudd, G. Dehm, C.H. Liebscher, Observations of grain-boundary phase transformations in an elemental metal, Nature 579 (2020) 375-378.

[8] L. Wang, Y. Zhang, Z. Zeng, H. Zhou, J. He, P. Liu, M. Chen, J. Han, D.J. Srolovitz, J. Teng, Y. Guo, G. Yang, D. Kong, E. Ma, Y. Hu, B. Yin, X. Huang, Z. Zhang, T. Zhu, X. Han, Tracking the sliding of grain boundaries at the atomic scale, Science 375 (2022) 1261-1265.
[9] Y. Tian, X. Gong, M. Xu, C. Qiu, Y. Han, Y. Bi, L.V. Estrada, E. Boltynjuk, H. Hahn, J. Han, D.J. Srolovitz, X. Pan, Grain rotation mechanisms in nanocrystalline materials: Multiscale observations in Pt thin films, Science 386 (2024) 49-54.
[10] R. Dang, Y.-W. Zhang, H. Gao, Predicting shear coupling behaviors in disconnection-mediated migration of asymmetrical tilt grain boundaries, International Journal of Plasticity 193 (2025) 104441.
[11] H. Grimmer, W. Bollmann, D.H. Warrington, Coincidence-site lattices and complete pattern-shift in cubic crystals, Acta Crystallographica Section A 30 (1974) 197-207.
[12] M. Wagih, C.A. Schuh, Viewpoint: Can symmetric tilt grain boundaries represent polycrystals?, Scripta Materialia 237 (2023) 115716.
[13] G.S. Rohrer, The distribution of grain boundary planes in polycrystals, JOM 59 (2007) 38-42.
[14] X.Y. Li, Z.H. Jin, X. Zhou, K. Lu, Constrained minimal-interface structures in polycrystalline copper with extremely fine grains, Science 370 (2020) 831-836.
[15] W. Xu, B. Zhang, K. Du, X.Y. Li, K. Lu, Thermally stable nanostructured Al-Mg alloy with relaxed grain boundaries, Acta Materialia 226 (2022) 117640.
[16] H. Fu, X. Zhou, Z. Gao, Z. Jin, X. Li, K. Lu, Effect of Grain Geometry on the Stability of Polycrystalline Pt at the Nanoscale, Physical Review Letters 134 (2025) 056101.
[17] C.A. Howells, Y. Mishin, Angular-dependent interatomic potential for the binary Ni–Cr system, Modelling and Simulation in Materials Science and Engineering 26 (2018) 085008.
[18] S. Plimpton, Fast parallel algorithms for short-range molecular dynamics, Journal of Computational Physics 117 (1995) 1-19.
[19] A. Stukowski, Visualization and analysis of atomistic simulation data with OVITO–the Open Visualization Tool, Modelling and Simulation in Materials Science and Engineering 18 (2010) 015012.
[20] Y. Si, Y. Zhang, D. Chen, J.L. Wormald, B.S. Anglin, D.L. McDowell, T. Zhu, Atomistic determination of Peierls barriers of dislocation glide in nickel, Journal of the Mechanics and Physics of Solids 178 (2023) 105359.
[21] T. Zhu, J. Li, A. Samanta, H.G. Kim, S. Suresh, Interfacial plasticity governs strain rate sensitivity and ductility in nanostructured metals, Proceedings of the National Academy of Sciences of the USA 104 (2007) 3031-3036.
[22] Y. Zhang, K. Ding, S. Stangebye, D. Chen, J. Kacher, O. Pierron, T. Zhu, Atomistic modeling of surface and grain boundary dislocation nucleation in FCC metals, Acta Materialia 237 (2022) 118155.
[23] S. Gupta, S. Stangebye, K. Jungjohann, B. Boyce, T. Zhu, J. Kacher, O.N. Pierron, In situ TEM measurement of activation volume in ultrafine grained gold, Nanoscale 12 (2020) 7146-7158.
[24] H. Conrad, Plastic deformation kinetics in nanocrystalline FCC metals based on the pile-up of dislocations, Nanotechnology 18 (2007) 325701.
[25] R. Bonnet, E. Cousineau, D.H. Warrington, Determination of near-coincident cells for hexagonal crystals. Related DSC lattices, Acta Crystallographica A37 (1981) 184-189.